

# Mesospheric vertical thermal structure and winds on Venus from HHSMT CO spectral-line observations

Miriam Rengel\*, Paul Hartogh, Christopher Jarchow

*Max-Planck-Institut für Sonnensystemforschung, Max-Planck-Strasse 2, 37191 Katlenburg-Lindau, Germany*

Received 29 January 2008; received in revised form 28 June 2008; accepted 1 July 2008

Available online 24 July 2008

## Abstract

We report vertical thermal structure and wind velocities in the Venusian mesosphere retrieved from carbon monoxide ( $^{12}\text{CO}$   $J = 2-1$  and  $^{13}\text{CO}$   $J = 2-1$ ) spectral line observations obtained with the Heinrich Hertz Submillimeter Telescope (HHSMT). We observed the mesosphere of Venus from two days after the second Messenger flyby of Venus (on 5 June 2007 at 23:10 UTC) during five days. Day-to-day and day-to-night temperature variations and short-term fluctuations of the mesospheric zonal flow were evident in our data. The extensive layer of warm air detected recently by SPICAV at 90–100 km altitude is also detected in the temperature profiles reported here.

These data were part of a coordinated ground-based Venus observational campaign in support of the ESA Venus Express mission. Furthermore, this study attempts to cross-calibrate space- and ground-based observations, to constrain radiative transfer and retrieval algorithms for planetary atmospheres, and to contribute to a more thorough understanding of the global patterns of circulation of the Venusian atmosphere.

© 2008 Elsevier Ltd. All rights reserved.

*Keywords:* Venus; Middle atmosphere

## 1. Introduction

Understanding the Venusian atmospheric dynamics is one of the fundamental problems in planetary sciences. Its study is of great value not only to learn about Venus itself, but also to interpret observations of extrasolar terrestrial planets, and among other examples, to understand their range of habitability. Two international missions recently joined efforts and carried out multi-point observations of the Venusian atmosphere on 6 June for several hours: NASA's MESSENGER spacecraft swung by Venus for a second time on 5 June 2007 at 23:10 UTC on its way to Mercury, and ESA's Venus Express is orbiting around Venus since 11 April 2006. Among the space-based observations, a world-wide coordinated Earth-based Venus observational campaign from 23 May 2007 to 9 June (and later) was initiated to remotely observe the Venusian

atmosphere.<sup>1</sup> Because Venus was close to its maximum eastern elongation during June 2007, Venus was in a favourable position for ground-based observations of both its day- and nightside.

The Venusian atmosphere is conventionally divided into three regions: the troposphere (below 70 km), the mesosphere (70–120 km), and the thermosphere (above 120 km). Studying the Venus' mesosphere dynamics is of special interest because this transition region is characterized by the combination of two different wind regimes (a retrograde super-rotation of the lower atmosphere, and a sub-solar to anti-solar flow pattern, SS–AS, of the upper atmosphere), and affects both the chemical stability and the thermal structure of the entire atmosphere (Clancy et al., 2003). The principal feature of Venus' atmospheric general circulation is the zonal super-rotation with typical wind velocities of 60–120  $\text{ms}^{-1}$  at the cloud top and nearly zero on the ground. An important (best measured) tracer of the atmospheric motion of Venus is carbon monoxide (CO)

\*Corresponding author. Tel.: +49 5556979244; fax: +49 5556979240.

E-mail address: [rengel@mps.mpg.de](mailto:rengel@mps.mpg.de) (M. Rengel).

URL: <http://www.mps.mpg.de/homes/rengel/> (M. Rengel).

<sup>1</sup><http://sci.esa.int/science-e/www/object/index.cfm?fobjectid=41012>.

(Kakar et al., 1976; Wilson et al., 1981). Sub-millimetre spectral line observations of CO and its isotopes play an important role in the investigation of the poorly constrained Venus mesosphere (it is the only technique to provide direct wind measurements in the mesosphere): they are used to retrieve vertical profiles of CO, temperature, and winds at the mesospheric altitudes (e.g., Clancy and Muhleman, 1991; Lellouch et al., 1994; Clancy et al., 2003; Rengel et al., 2008).

Data capabilities and partial preliminary results from the submillimetre observations of the CO lines carried out with the Heinrich Hertz Submillimeter Telescope (HHSMT) during June 2007 on the mesosphere of Venus as a part of the ground-based observing campaign were reported in Rengel et al. (2008).

In this paper, we present a complete retrieval analysis of the data obtained, and report of mesospheric parameters such as wind, vertical thermal structure, and CO abundance derived from the  $^{12}\text{CO}$   $J = 2-1$  and  $^{13}\text{CO}$   $J = 2-1$  lines by the use of a radiative transfer model and retrieval algorithm. Section 2 summarizes the observations and describes the data reduction. The results are presented in Section 3. Spacial/temporal changes in the mesospheric thermal structure and winds are discussed in Section 4.

## 2. Observations and data reduction

CO observations on the disc of Venus were carried out at the HHSMT, operated and owned by the Arizona Radio Observatory (ARO). The telescope is located at an elevation of 3178 m on Mount Graham, Arizona, and consists of a 10-m diameter primary with a nutating secondary. Our 8, 9, 10, 14 and 15 June from 18:30 to 0:30 UT observations employed the 345 Superconductor-Insulator Superconductor (SIS) and the 2 mmJT/1.3 mmJT ALMA Sideband Separating<sup>2</sup> receivers, operating, respectively, at 320–375 and 210–279 GHz to observe the  $^{12}\text{CO}$   $J = 2-1$  (at a frequency of 230.54 GHz),  $^{12}\text{CO}$   $J = 3-2$  (at 345.79 GHz), and  $^{13}\text{CO}$   $J = 2-1$  (at 220.398 GHz) rotational transitions. The 345 SIS double sideband receiver was used with the signal frequency being placed once in the lower sideband (LSB) and another time in the upper sideband (USB), and the 2 mmJT/1.3 mmJT one only in LSB. We used simultaneously seven different backends: two 1 MHz Forbes filterbanks (FFBA and FFBB), two 970 MHz wide acousto-optical spectrometers (AOSA and AOSB, with mean resolutions of 934 kHz for AOSA and 913 kHz for AOSB), two FB2 (FB2A and FB2B) filter-backends, and one 215 MHz CHIRP transform spectrometer (CTS, resolution of  $\sim 40$  kHz) (Hartogh and Hartmann, 1990; Villanueva and Hartogh, 2006).

<sup>2</sup>Developed as part of the ALMA project, this system is the first of this kind to incorporate the latest SIS mixer technology: image-separating mixers. Here, the image-separating system operates truly separating image noise and signal. It uses an old 1.3 and 2 mm quasioptical JT Dewar and cross-grid to separate the two orthogonal linear polarizations.

Observing conditions were generally good, although on 10, 14 and 15 June it was partially cloudy. System temperatures were typically 1500–2500 for the 345 GHz receiver and 200–500 K for the 2 mmJT/1.3 mmJT receiver. The observing mode was always dual beam switching. Pointing was checked every 2–3 h. The typical integration time per individual spectrum was around 4 min.

The Venus disc had a diameter of 23.44" at the beginning and 25.55" at the end of our observational period, with the evening terminator separating the dayside crescent (the fraction of illumination for Venus was 49.95 and 45.68%, as seen by observer). Fig. 1 in Rengel et al. (2008) shows a synthetic image of the apparent disc of Venus that approximates the telescopic view of Venus as seen from the Earth at 8 June and 18:30 UT.

An overview of the complete data set can be found in Rengel et al. (2008). We obtained measurements for  $^{12}\text{CO}$   $J = 2-1$  at seven positions (including centre, east and west limbs on the Venus disc) and for  $^{13}\text{CO}$   $J = 2-1$  at one (centre), see Fig. 1. The retrieval of the temperature profile and winds requires a clean spectrum (spectrum with minor or almost zero baseline features), and the CTS with a high dynamical range larger than 30 dB is well suited for our goals, here we concentrate only on the data taken with the CTS. The  $^{12}\text{CO}$   $J = 3-2$  line observations were substantially noisier than  $^{12}\text{CO}$   $J = 2-1$ , so they are not considered in our analysis here. Table 1 gives a summary of our  $^{12}\text{CO}$   $J = 2-1$  and  $^{13}\text{CO}$   $J = 2-1$  observations.

The initial reduction of each spectrum was performed using the CLASS software package of the Grenoble Astrophysics Group.<sup>3</sup>

## 3. Data analysis: retrieval of mesospheric parameters (vertical thermal structure, CO abundance, and winds)

### 3.1. Vertical thermal structure and CO profile

In order to retrieve the temperature profile in the mesosphere, we have applied a retrieval technique described by C. D. Rodgers as optimal estimation (Rodgers, 1976). We used a radiative transfer code (Jarchow and Hartogh, 1995; Jarchow, 1998; Hartogh and Jarchow, 2004) which describes the physics of the radiative transfer through the atmosphere, i.e., describes the transport and balance of energy within the atmosphere, to calculate the synthetic spectra which best fit the observed spectra. And a priori profile is required as initial input for the optimal estimation technique. A priori atmospheric temperature profiles, for day and nightsides, were taken from the Venus international reference atmosphere (VIRA) (Kliore et al., 1992). For observations centred on the evening terminator, a uniform profile at 172 K at altitudes higher than 90 km was considered as approximation (and the VIRA profile at altitudes lower than 90 km). The a priori CO vertical profile employed is described in the paragraph below. For the

<sup>3</sup><http://www.iram.fr/IRAMFR/GILDAS>.

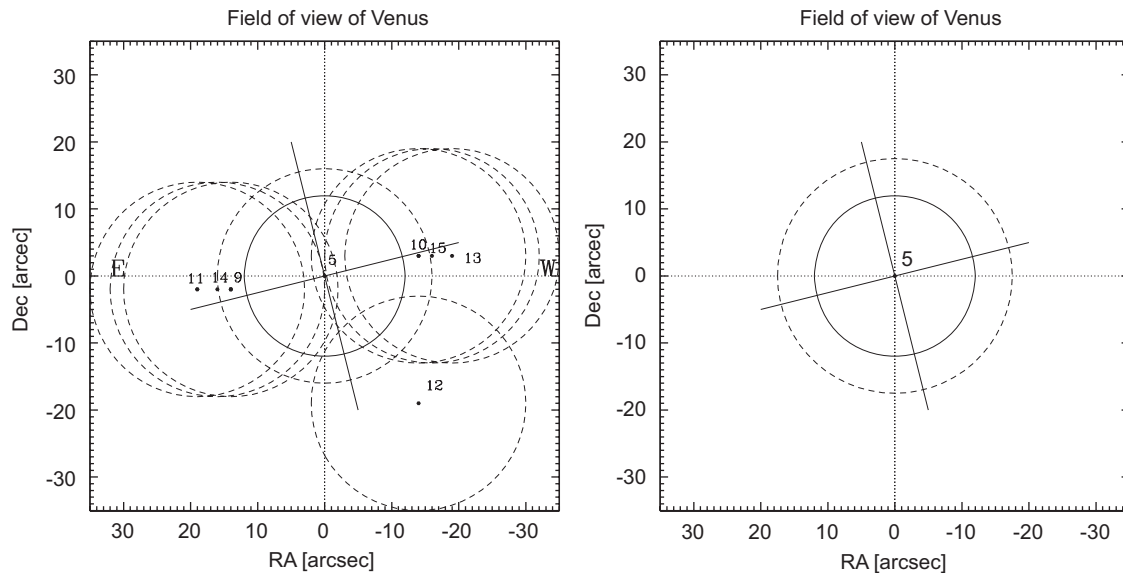


Fig. 1. Schematic of the beam locations on the Venus disc (for a 24'' disc diameter) where  $^{12}\text{CO}$   $J = 2-1$  and  $^{12}\text{CO}$   $J = 3-2$  line integrations are obtained (left and right panels, respectively). Solid lines indicate the Venus' equator and central meridian. Dashed circles indicate the approximate FWHM beam diameter.

Table 1  
Observation parameters for the  $^{12}\text{CO}$   $J = 2-1$  line

Beam position	$d\alpha^a$	$d\delta^a$	Obs. no.	Scan no.	Line	Date (June 2007)	Receiver/sideband
5	0	0	19	139–140	$^{12}\text{CO}$ $J = 2-1$	14	2 mm/1.3 mm ALMA–LSB
9	14	–2	20	141–146	$^{12}\text{CO}$ $J = 2-1$	14	2 mm/1.3 mm ALMA–LSB
10	–14	3	21	147–152	$^{12}\text{CO}$ $J = 2-1$	14	2 mm/1.3 mm ALMA–LSB
9	14	–2	22	153–156	$^{12}\text{CO}$ $J = 2-1$	14	2 mm/1.3 mm ALMA–LSB
5	0	0	23	164–165	$^{12}\text{CO}$ $J = 2-1$	14	2 mm/1.3 mm ALMA–LSB
9	14	–2	24	166–167	$^{12}\text{CO}$ $J = 2-1$	14	2 mm/1.3 mm ALMA–LSB
11	19	–2	25	168–173	$^{12}\text{CO}$ $J = 2-1$	14	2 mm/1.3 mm ALMA–LSB
12	–14	–19	26	174–176	$^{12}\text{CO}$ $J = 2-1$	14	2 mm/1.3 mm ALMA–LSB
11	19	–2	27	177–182	$^{12}\text{CO}$ $J = 2-1$	14	2 mm/1.3 mm ALMA–LSB
13	–19	3	28	183–188	$^{12}\text{CO}$ $J = 2-1$	14	2 mm/1.3 mm ALMA–LSB
10	–14	3	29	189–194	$^{12}\text{CO}$ $J = 2-1$	14	2 mm/1.3 mm ALMA–LSB
5	0	0	30	195–196	$^{12}\text{CO}$ $J = 2-1$	14	2 mm/1.3 mm ALMA–LSB
5	0	0	31	199–202	$^{13}\text{CO}$ $J = 2-1$	14	2 mm/1.3 mm ALMA–LSB
5	0	0	32	208–217	$^{12}\text{CO}$ $J = 2-1$	15	2 mm/1.3 mm ALMA–LSB
14	16	–2	33	218–227	$^{12}\text{CO}$ $J = 2-1$	15	2 mm/1.3 mm ALMA–LSB
15	–16	3	34	228–237	$^{12}\text{CO}$ $J = 2-1$	15	2 mm/1.3 mm ALMA–LSB
5	0	0	35	244–293	$^{13}\text{CO}$ $J = 2-1$	15	2 mm/1.3 mm ALMA–LSB
5	0	0	36	295–299	$^{12}\text{CO}$ $J = 2-1$	15	2 mm/1.3 mm ALMA–LSB

<sup>a</sup> $d\alpha$  and  $d\delta$ , right ascension and declination, are the astronomical coordinates of a point on the celestial sphere when using the equatorial coordinate system. The earlier coordinate is the celestial equivalent of terrestrial longitude, and the later one, to the latitude, projected onto the celestial sphere.

analysis here these profiles were automatically included in the points distributed throughout the disc (Fig. 2). Fig. 2 shows how we calculated the disc-averaged spectrum. For each black dot a pencil beam spectrum (convolved with the telescope 2D Gaussian beam pattern) has been calculated. The rings show the grouping of the dots. Within a ring each dot has the same distance from the centre of the planetary disc. The density of the dots has been chosen according to the variation of the spectra: low density at the disc centre and high density at the limb, because the spectra of the

single pencil beams vary only slowly at the centre, while due to the exponential density decrease of the atmosphere with altitude the limb area has to be resolved much higher. We sub-divided the limb area into 16 rings to model accurately the contribution of the limb region to the disc-averaged spectra.

Our atmospheric model consisted of 46 layers spanning the 30–120 km interval with a resolution of 2 km. Upwelling continuum emission from the  $\sim 55$  km altitude region is modelled by incorporating the collision induced absorption

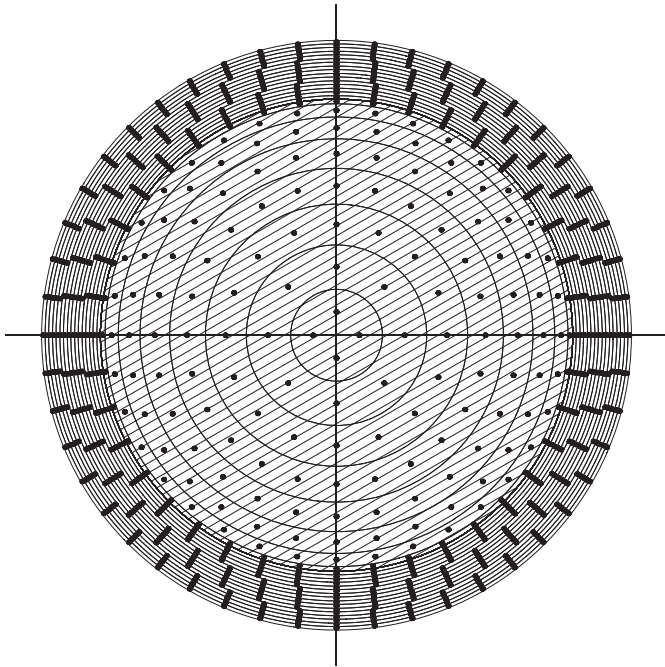


Fig. 2. Schematic representation of the Venus disc showing the distribution of the points where a pencil beam spectrum has been calculated. The rings show the grouping of the dots. Within a ring each dot has the same distance from the centre of the Venus disc. Limb area is not to scale with respect to the disc. Shade area represents the disc corresponding to the solid body.

of CO<sub>2</sub> (Gruszka and Borysow, 1997) and using the VIRI temperature data at this altitude. Initially, the observed spectra were modelled in units of percent absorption and then converted to absolute brightness temperature by rescaling the spectra in such a way that the continuum brightness temperature equal to the VIRI temperature around 55 km.

We derived the CO mixing ratio profile from the simultaneous fitting of <sup>12</sup>CO J = 2–1 and <sup>13</sup>CO J = 2–1 HHSMT spectra (Fig. 10, Obs. 35 and 36). Both observations constrain CO abundances over different ranges of altitude since they have a different opacity. Two lines of the same molecule with strongly different altitude dependent opacity allow retrieving simultaneously the vertical profiles of temperature and its volume mixing ratio. Unfortunately we have only two cases in which we observed two lines at the same time. Obs. 35, pointing only at the disc centre was the least noisy one. We decided to retrieve the vertical profile of CO from this observation and use it as a priori profile for all other retrievals presented in this paper. We stress that simultaneous temperature/CO retrievals are less reliable when only <sup>12</sup>CO J = 2–1 data are available. The mentioned solely joint retrieval employed as a priori a CO mixing ratio profile purely increasing exponentially with the altitude, a profile similar to the average of the profiles of Fig. 8A–B in Clancy and Muhleman (1991). Note that we did not fix the CO profile with zero error in the temperature from a single CO spectra line observation but left error bars unequal zero on it, i.e.,

the error bars we got from the CO retrieval. The reason not to fix the CO profile in the retrieval (error bars zero) is that in reality the CO profile is variable and each measurement, even with highest accuracy is just a snapshot for the moment of the observation. In other words, for a single <sup>12</sup>CO line observation we give the fit algorithm the freedom to not only fit the temperature profile, but to a small extent also the CO profile. However, while for the CO profile retrieval with two lines the correlation length for the CO profile was only 10 km (providing almost the same vertical resolution) in the case of a single line retrieval the correlation length has been set to 40 km. In other words, the fit algorithm can hardly modify the (exponential) shape of the CO-profile, but almost just shift it forth and back as a whole within the (relatively small) error bars.

The capability of the fitting algorithm to retrieve the atmospheric temperature, CO-profile, and winds can be characterized by the so-called weighting functions  $K_x$  as defined by Rodgers (1990). Here we briefly present the procedure we followed in order to calculate  $K_x$ . Representing the atmosphere by a set of  $N$  layers allows to write the atmospheric profiles as a state vector  $x$ , where  $x$  is a vector of unknowns to be retrieved from the measurements  $y$ .  $y$  is a vector of measured quantities (i.e., the CO spectrum measured at  $m$  discrete frequencies). The so-called forward model  $F(x)$  relates  $x$  to  $y$  as  $y = F(x)$ . This forward model contains the complete physics necessary to calculate the absorption coefficient as a function of temperature, mixing ratio, and spectral line parameters, and in addition performs the radiation transfer through the atmosphere. It is in general a non-linear function of the vector  $x$  of unknowns.

The weighting functions  $K_x$  are now defined as  $K_x = \partial F(x)/\partial x$ . They describe the sensitivity of the measurement, which means the observed CO spectrum, with respect to each single parameter to be retrieved. Using  $K_x$  allows to linearize the forward model around a reference state  $\bar{x}$ :

$$y = F(\bar{x}) + \frac{\partial F(\bar{x})}{\partial x} \cdot (x - \bar{x}). \quad (1)$$

For the calculation of  $K_x$  here we used as reference state the a priori profiles and normalized the resulting curves to unity as maximum value. Because the measurement depends in a different way on atmospheric temperature and CO mixing ratio, the weighting functions have to be different for the temperature and mixing ratio. As seen later, this is most strikingly visible at the altitude around 55 km: here the collision induced absorption of CO<sub>2</sub> in Venus atmosphere creates a sensitivity of the spectrum with respect to temperature, independent of the CO mixing ratio. On the other hand, the spectrum is not sensitive to the CO mixing ratio around this altitude anymore, because the same CO<sub>2</sub> absorption lets the atmosphere become optically thick below 55 km. Finally, if the weighting functions are zero in a certain altitude range this means

here the observation does not depend on the atmospheric parameters, and consequently there parameters cannot be retrieved at this altitude range.

Introducing the inverse model  $I$ , which relates the retrieved atmospheric state  $\hat{x}$  to  $y$ ,  $\hat{x} = I(y)$ , and combining it with the forward model  $y = F(x)$ , allows to

define a transfer function  $T$ :

$$\hat{x} = I(F(x)) = T(x). \tag{2}$$

The averaging kernels  $A$  are now defined as  $A = \partial T(x)/\partial x$  and describe the sensitivity of the retrieved atmospheric parameters with respect to each single true parameter.

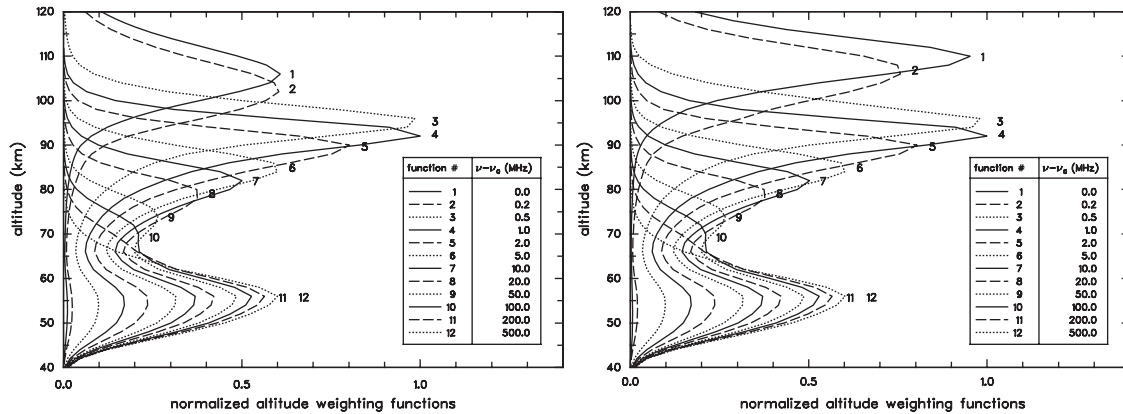


Fig. 3. Dayside (left) and nightside (right) normalized atmospheric temperature weighting functions as provided by  $^{12}\text{CO}$   $J = 2-1$  line. Each function corresponds to a particular frequency offset from line centre (from 0 to 500 MHz offset).

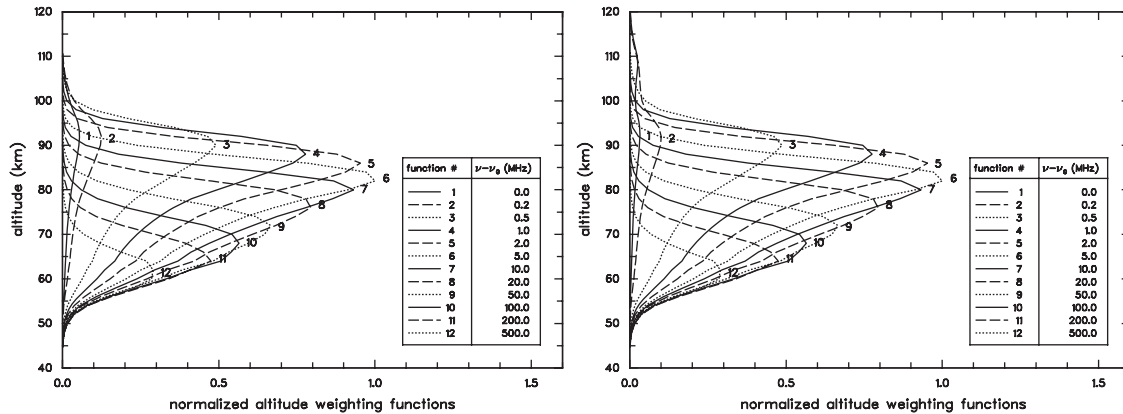


Fig. 4. Dayside (left) and nightside (right) normalized CO mixing weighting functions as provided by  $^{12}\text{CO}$   $J = 2-1$  line. Each function corresponds to a particular frequency offset from line centre (from 0 to 500 MHz offset).

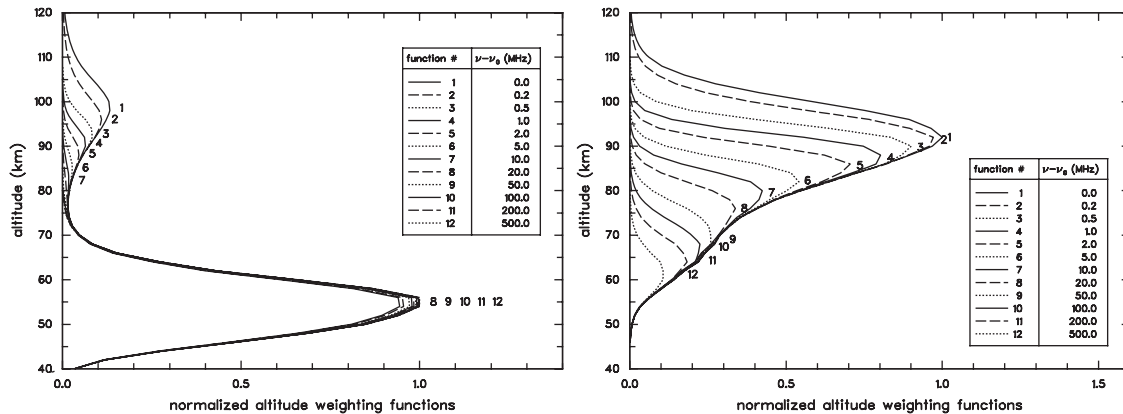


Fig. 5. Temperature (left) and CO mixing weighting functions (right) as provided by  $^{13}\text{CO}$   $J = 2-1$  line. Each function corresponds to a particular frequency offset from line centre (from 0 to 500 MHz offset).

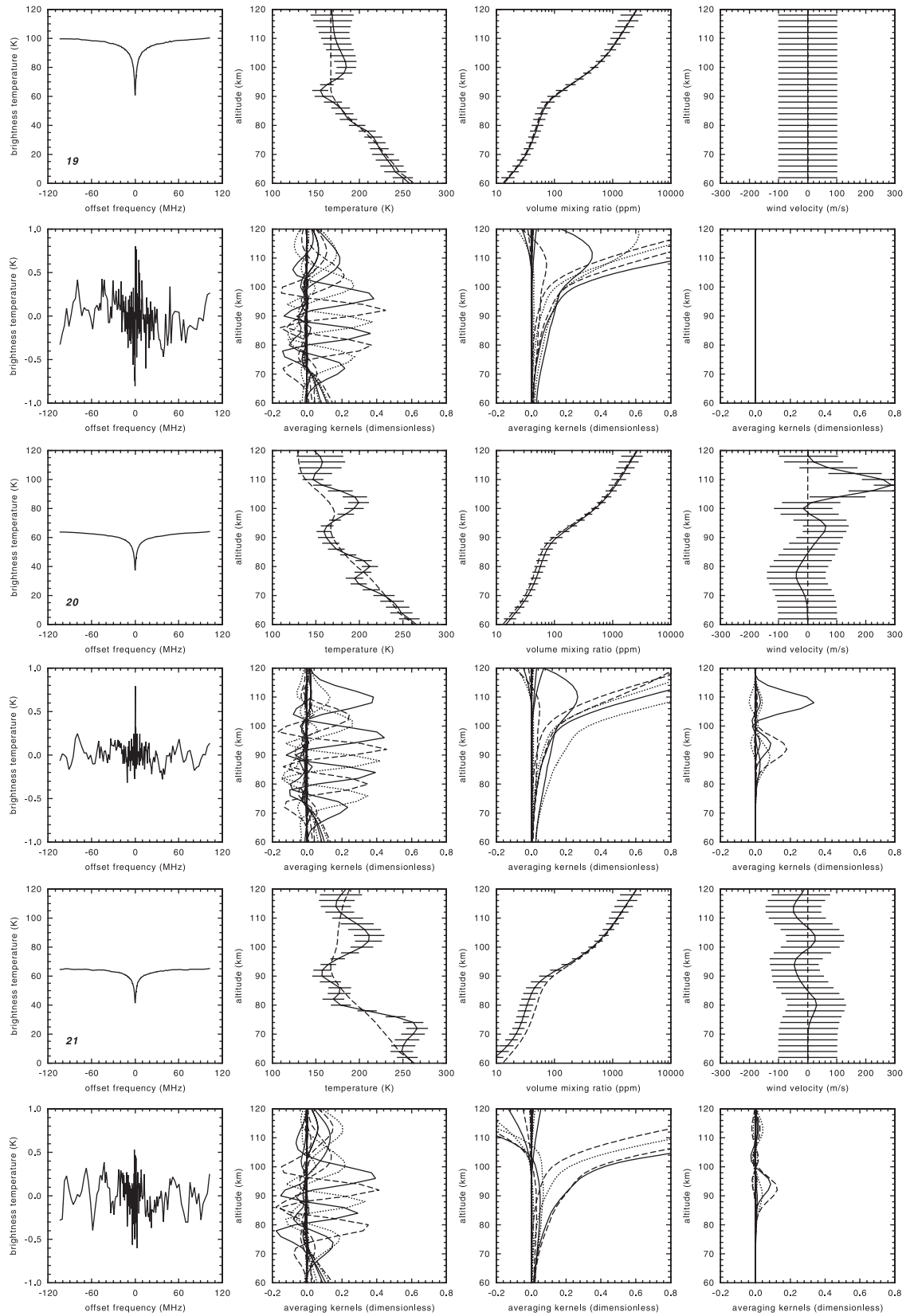


Fig. 6. Synthetic spectra solution for observations in Table 1 (left upper panels), difference between the observed and fitted spectra (left lower panels), retrieved temperature, CO distribution and wind derived from the spectrum. The dash lines show the initial profiles, and the horizontal lines the error bars.

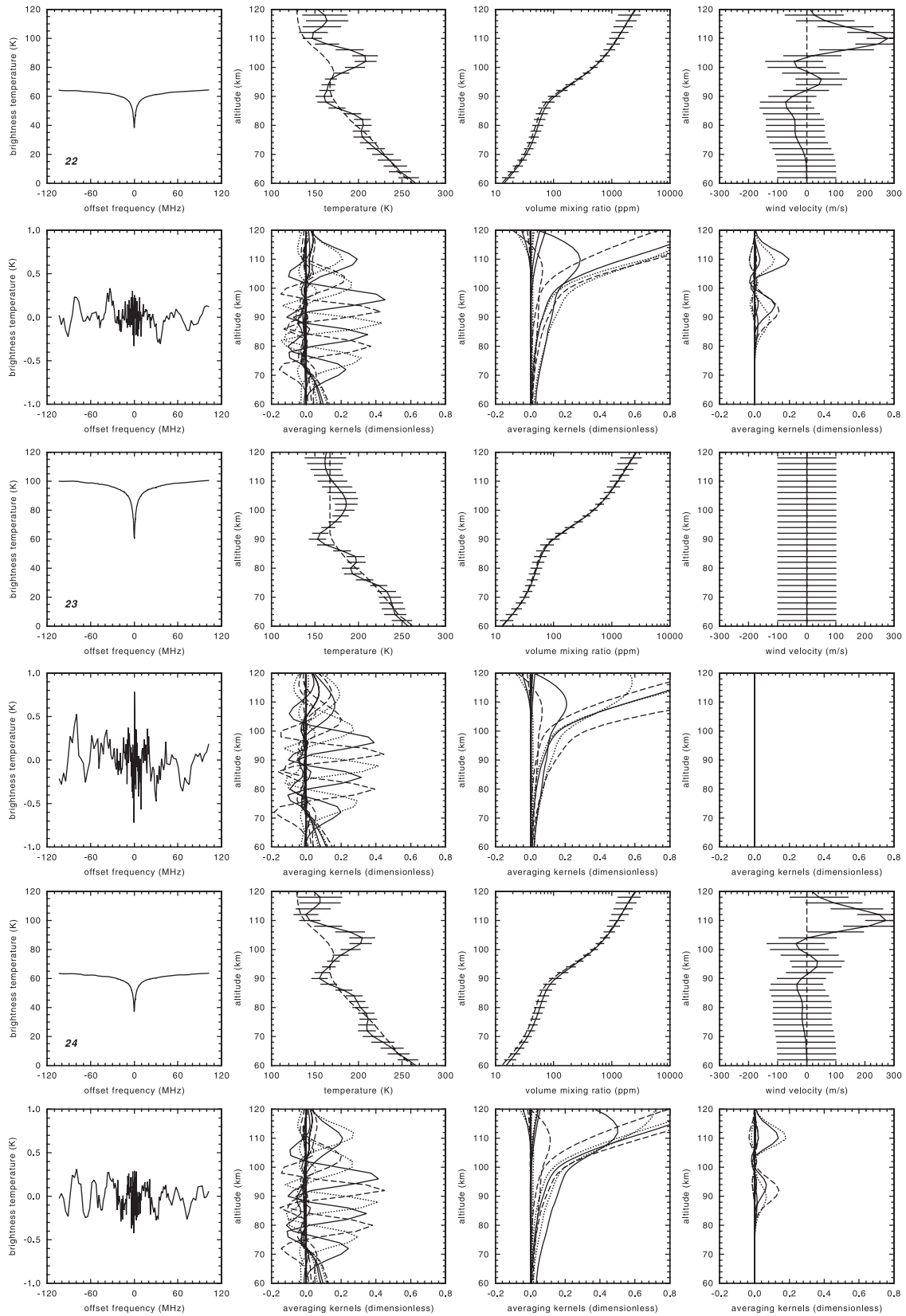


Fig. 7.

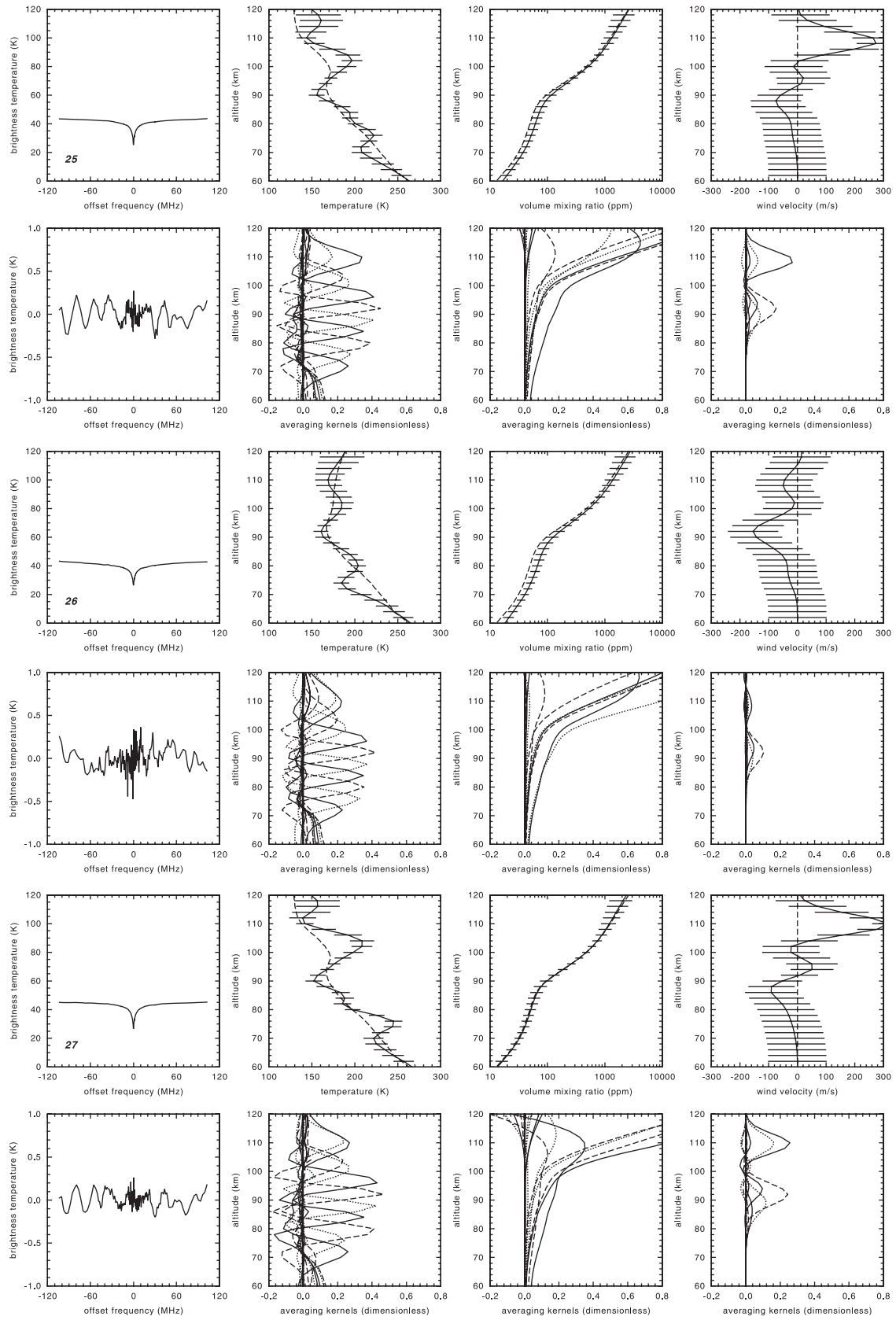


Fig. 8.

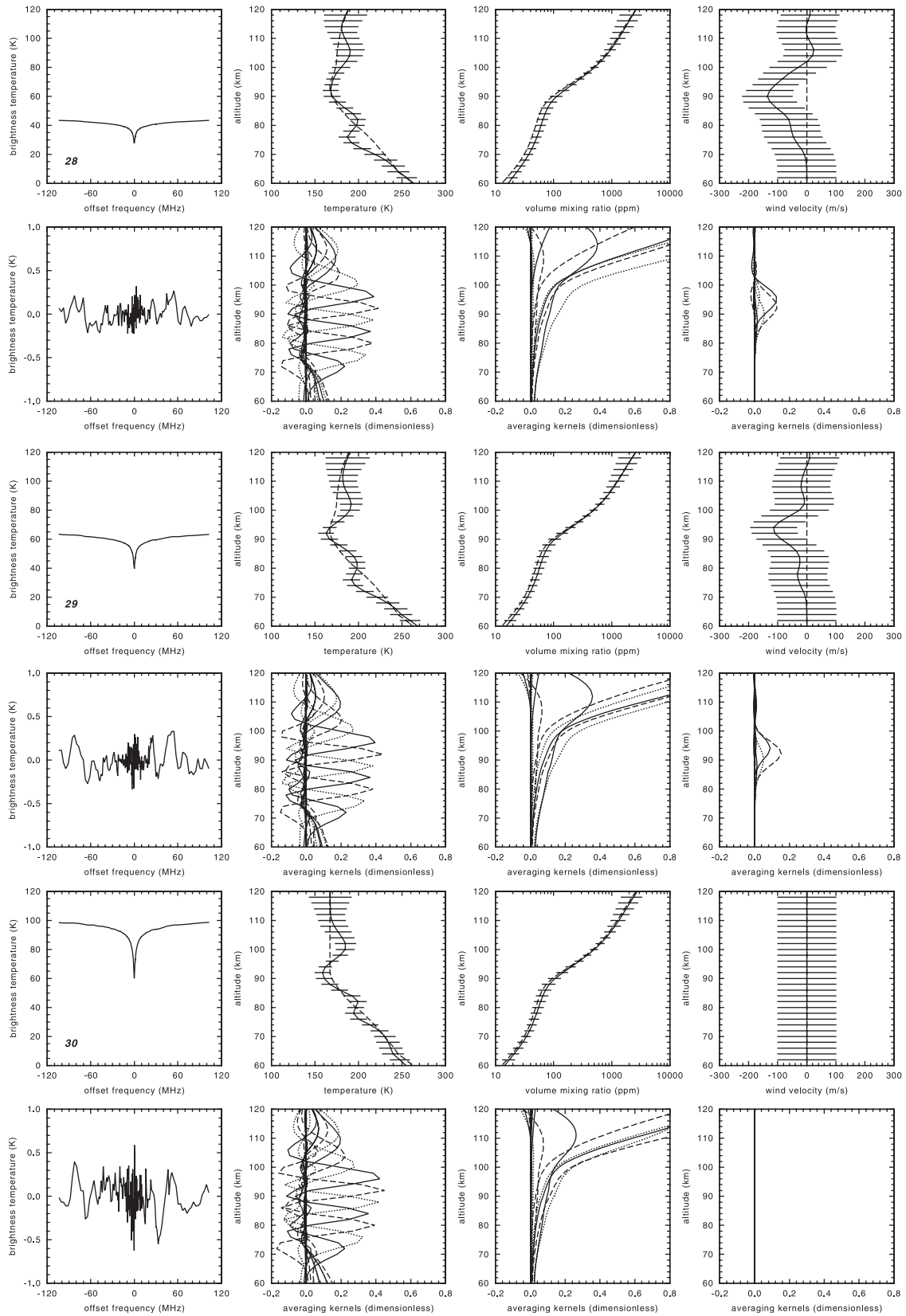


Fig. 9.

For each parameter, for example, a temperature at a certain altitude, there is an averaging kernel function, showing that this temperature depends on a change of the true temperature at all other altitudes.

Normalized temperature and CO-weighting functions for  $^{12}\text{CO}$   $J = 2-1$  (with separate panels for the nightside and dayside) and  $^{13}\text{CO}$   $J = 2-1$  for several frequency offsets around each transition are presented in Figs. 3 and 4, and in Fig. 5, respectively. They show the vertical range and resolution of temperature and of CO retrievals afforded here: temperature sensitivity for  $^{12}\text{CO}$   $J = 2-1$  is primarily confined to the 55–110 km range,  $^{12}\text{CO}$   $J = 2-1$

sensitivity to 68–90 km range, temperature sensitivity for  $^{13}\text{CO}$   $J = 2-1$  to 55–100 km range, and  $^{13}\text{CO}$   $J = 2-1$  sensitivity to 70–95 km range. Because of the input CO profile, the vertical distribution of the CO weighting functions in Fig. 4 are not greatly influenced by day-to-night variation of CO abundances. However, the divergence of day and night temperature profiles creates significant offsets in day and night altitude scales above 90 km altitude.

In Figs. 6–11 we present the measured and fitted spectra, and retrieved temperature profiles and CO distribution for the observations in Table 1 obtained with our technique

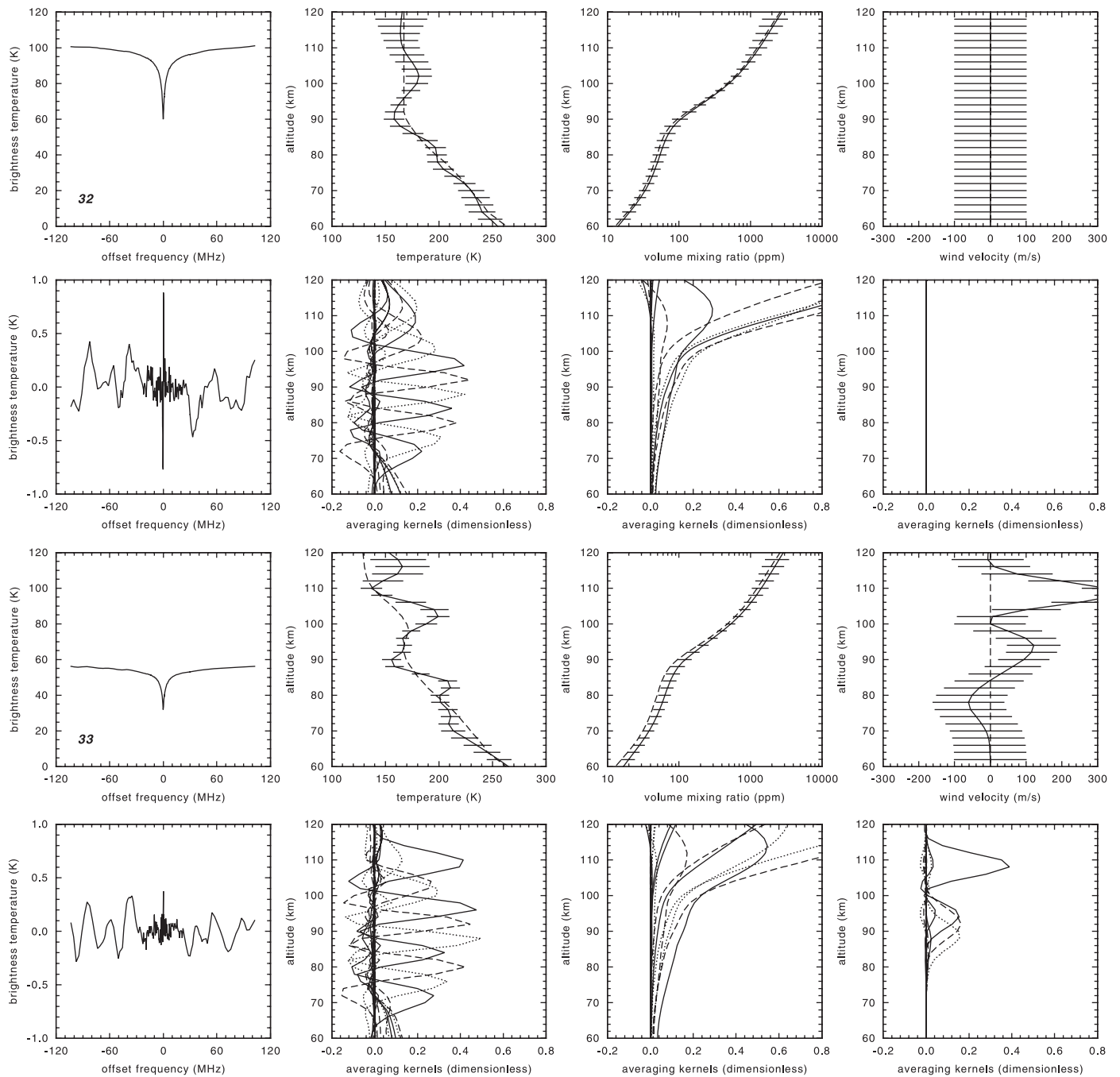


Fig. 10.

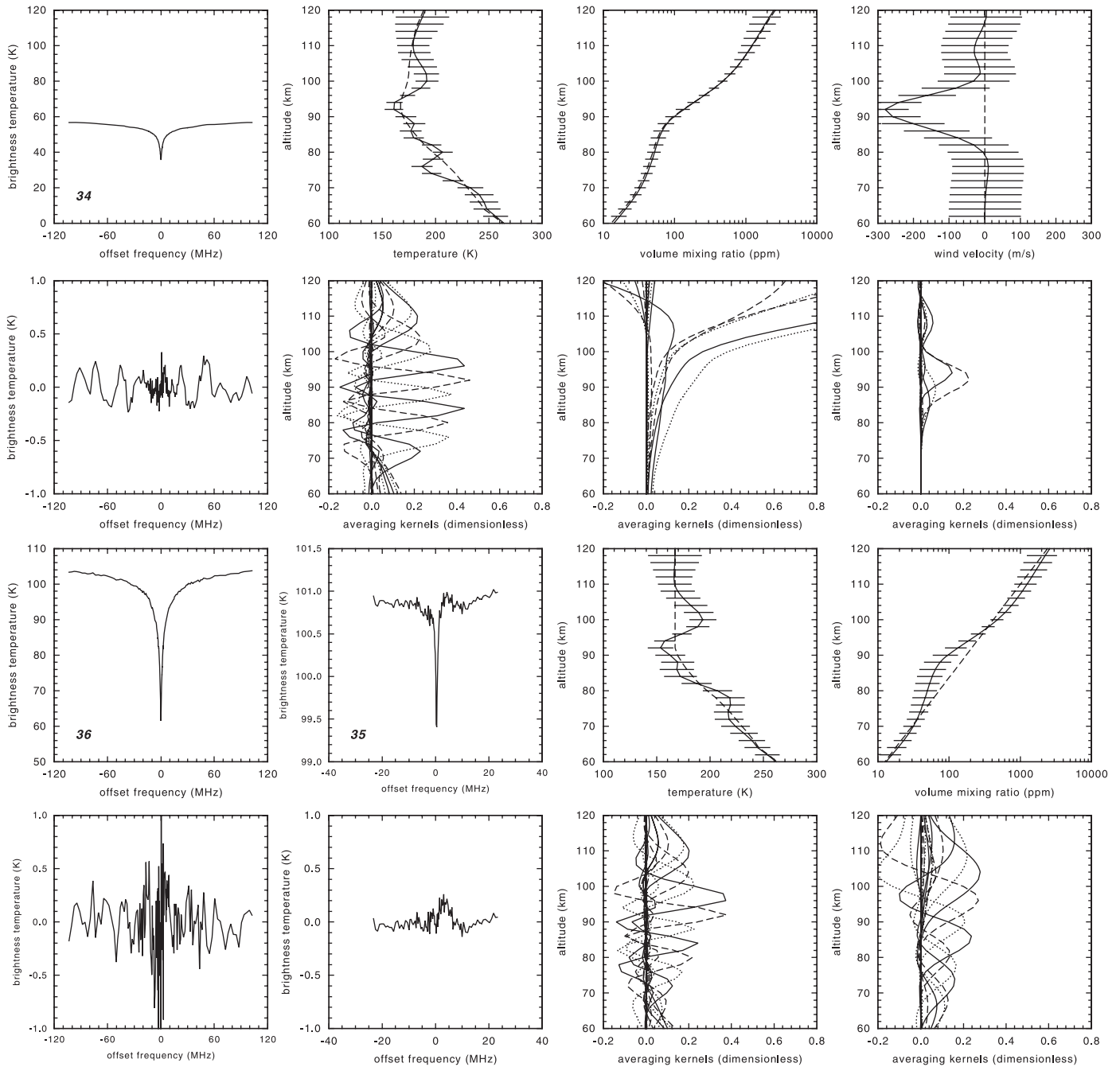


Fig. 11.

(Figs. 6–10 and 11 (upper panels) for  $^{12}\text{CO}$   $J=2-1$  and Fig. 11 (lower panels) for  $^{13}\text{CO}$   $J=2-1$  lines). Lower panels from the spectra boxes in Figs. 6–11 show difference between the observed and fitted spectra, and averaging kernels for temperature, CO, and winds, respectively. Note that the differences between the measured and fitted spectra are so small that they are hardly distinguished when they are plotted simultaneously. For clarity we show only each second averaging kernel curve. Wind retrieval will be addressed in the next section. Error bars represent the total error in the retrieval which comprises the contributions of measurement errors, model errors, and

null-space errors due to the inherent finite vertical resolution, as described in Rodgers (1990). These error terms appear as covariance matrices (interpreted in terms of error patterns) and are equivalent to error bars. The contribution of a priori to the retrieval is described in terms of the eigenvectors of the averaging kernel matrix. For the error bar calculations we followed the recipe given in Rodgers (1990). A discussion of the correlated errors can be found in Section 3.3.

The 15 June 2007 temperature profile from Obs. 36, for example, is compared with the ones obtained from SPICAV onboard Venus Express (Bertaux et al., 2007),

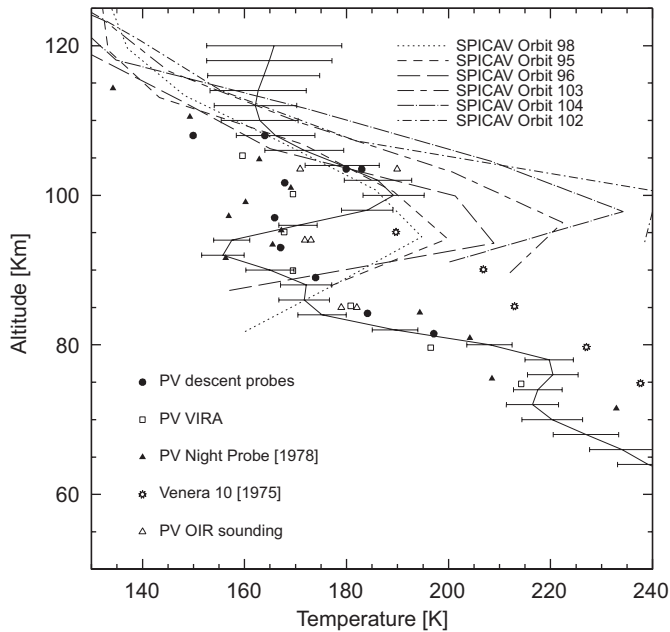


Fig. 12. Temperature profile retrieval (from Obs. 36), solid line, compared to the profile from the stellar occultations with the SPICAV onboard Venus Express (Bertaux et al., 2007), PV descent probes (Seiff et al., 1980), from the OIR sounding measurements (Schofield and Taylor, 1983), and from the PV night probe (Seiff and Kirk, 1982). The SPICAV measurements were taken at latitude  $39^{\circ}\text{N}$  for orbits 95, 96, and 98, and latitude  $4^{\circ}\text{S}$  for orbits 102–104. The Pioneer-Venus derived VIRA reference profile for latitudes  $<30$  are indicated by the squares. The anomalously warm temperatures returned by the Venera 10 probe in 1975 are shown as stars symbols. The absolute uncertainty for the temperatures derived here is  $\pm 15\text{K}$ .

Pioneer Venus (PV) descent probes (Seiff et al., 1980), to the OIR sounding measurements (Schofield and Taylor, 1983), and to the PV night probe (Seiff and Kirk, 1982) (Fig. 12). We detected a temperature excess at 90–100 km altitude which coincides with the extensive layer of warm air at altitudes 90–120 km detected by SPICAV (Bertaux et al., 2007). However, its peak shows a smaller temperature excess than the one detected by SPICAV. This particular layer has been interpreted as the result of adiabatic heating during air subsidence. Because adiabatic heating is a localized phenomenon, does the layer's altitude increase with the latitude? We note that layers' altitudes of around 95, 97 and 100 km are determined at latitudes of  $4^{\circ}\text{S}$ ,  $0^{\circ}$ , and  $39^{\circ}\text{N}$ , respectively (Bertaux et al., 2007; this work). We stress this possibility, however, three-point statistics cannot make a strong statement, additional data at different latitudes are required. Furthermore, in other altitudes the HHSMT profile compares favourably to those returned by the previous measurements. Similar temperature profiles were also observed (Lellouch et al., 1994; Clancy et al., 2003). Moreover, it was suggested that a 10–15 K increase in the mesospheric temperatures occur over 1–30-day periods, and large variations (20–40 K) over as yet undetermined timescales (Clancy et al., 2003). More data over longer periods are necessary.

### 3.2. Wind velocity retrieval

Fig. 13 shows the observed and fitted spectrum of  $^{12}\text{CO}$   $J=2-1$  (Obs. 27), the residual (difference between observation and fit), and the retrieved vertical temperature of CO profiles and respective kernels. The double peak in the centre of the residuum (left lower panel) shows that the fit between the observed and synthetic spectra has deviations, meaning that some physical parameters are still being missing in the model. Obviously, this double peak is related to a frequency shift of the fitted line relative to the observed one. This frequency shift is caused by movements of the observed air mass along the line of sight. In other words, we see the effect of winds causing Doppler shifts in the centre of the observed spectrum. In order to get a perfect fit an additional fit parameter has to be introduced, which minimizes the residual by frequency shifting the spectrometer channels around the line centre related to the wind speed as function of altitude. In more detail, we retrieved the beam-integrated wind velocities taking into account vertical information. The model assumes an individual uniform zonal wind speed within each atmospheric layer, and the layers together rotate with individual angular velocities among a common axis, the rotational axis of Venus. According to the component of the wind velocity vector along the line of sight, each location on the Venus' disc has its own Doppler shift: it is maximum at the limb on the equator, and zero for all points of the Venus' disc falling onto the rotational axis. Because the size of the main beam here is comparable to the diameter of the Venus' disc for our observational period, we integrated across the Venus' disc (see Fig. 2 and explanation in the last chapter) to take into account the smoothly varying Doppler shifts. Pointing exactly to the centre of the disc just causes the spectral line slightly to broaden, because the contributions from the western and eastern limb are Doppler-shifted with respect to the line centre, but in opposite directions. However, pointing to the eastern with respect to western limb causes the contribution from this limb to dominate over the contribution from the opposite limb (larger weight due to the antenna pattern) and the resulting spectral line appears to be completely red, respectively, blue shifted. This shift with respect to the nominal line centre is sufficient to retrieve a wind velocity within each individual atmospheric shell. As a priori profile we have chosen a wind speed of  $0\text{ m s}^{-1}$  throughout the whole atmosphere, with a standard deviation of  $100\text{ m s}^{-1}$ . The information gained by the observations will reduce the error bars in the altitude range the observations are sensitive to. Both, the upper and the lower boundary are related to spectral noise. If it exceeds a certain value, the retrieval algorithm cannot relate Doppler shifts to wind speeds smaller than  $100\text{ m s}^{-1}$ . Concerning the wind profile vertical resolution we have assumed a correlation between the layers characterized by a correlation length of 4 km (Rodgers, 1990). This value is similar to the one assumed for the temperature profile resolution (for the CO mixing

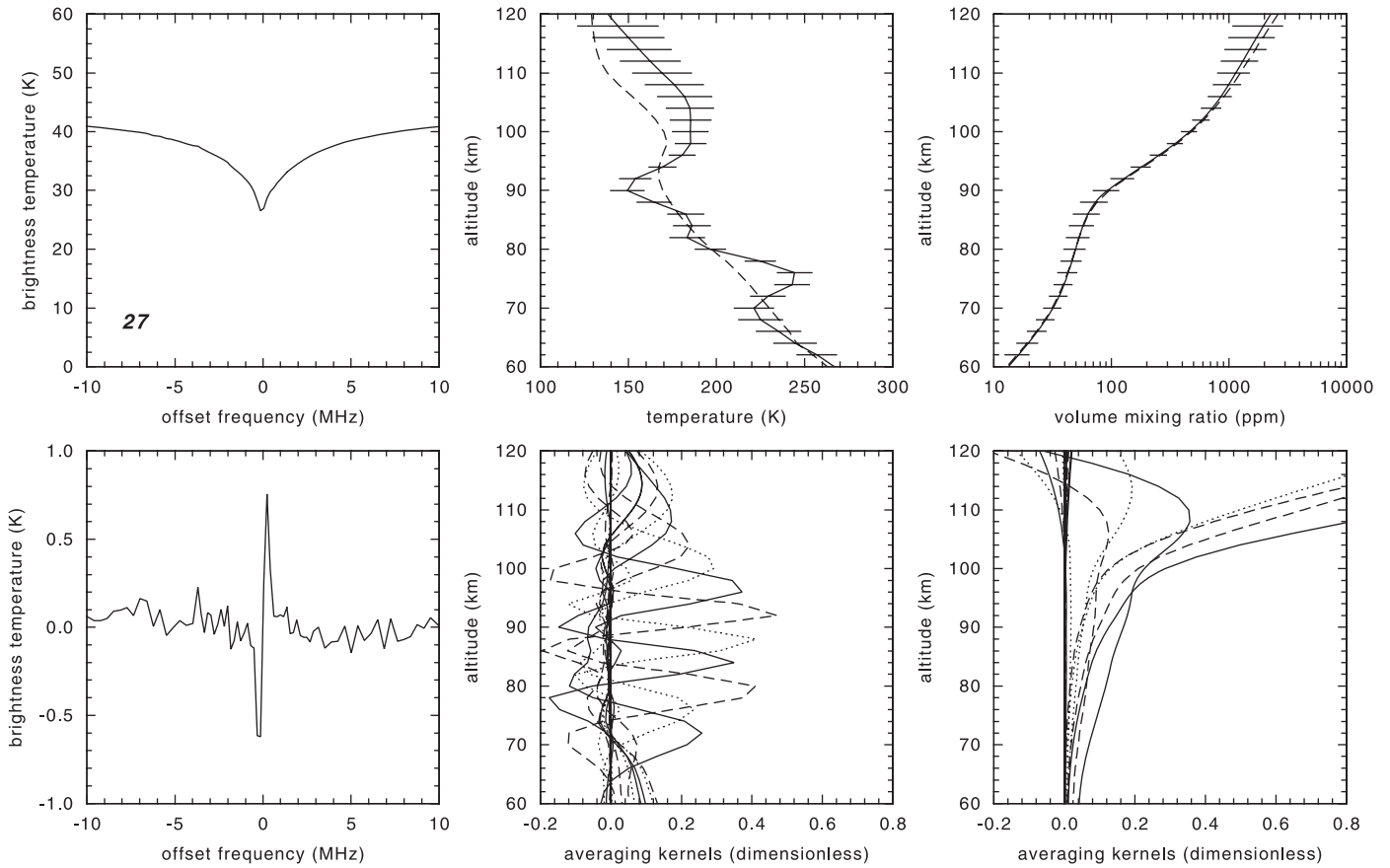


Fig. 13. Observed and fitted spectrum of  $^{12}\text{CO } J = 2-1$  (Obs. 27, top left panel), the residual (difference between observation and fit, bottom left panel), and the retrieved vertical temperature and CO profiles (top centre and right panels) and respective kernels (low centre and right panels). The double peak in the centre of the residuum (left lower panel) is related to a frequency shift of the fitted line relative to the observed one: effect of winds causing Doppler shifts in the centre of the observed spectrum.

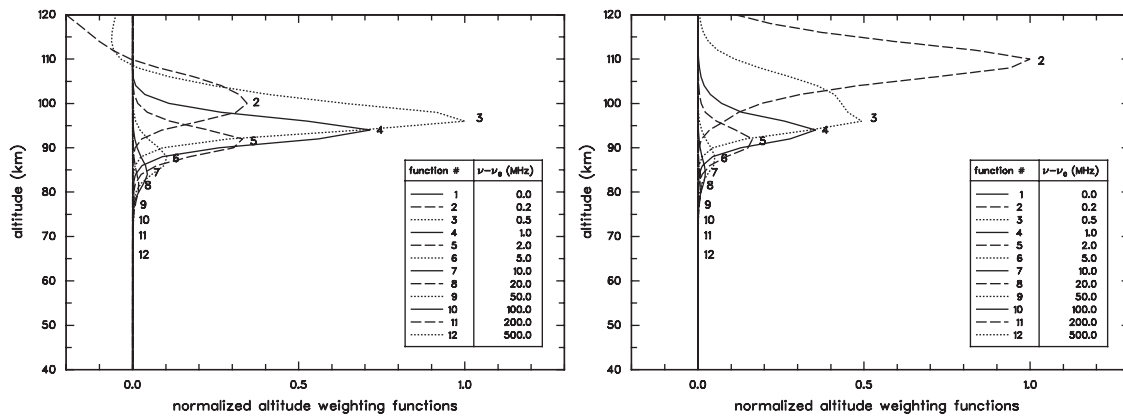


Fig. 14. Dayside (left) and nightside (right) wind weighting functions as provided by  $^{12}\text{CO } J = 2-1$  lines.

ratio we assumed higher values than these ones in order to restrict the degrees of freedom of the fitting). Wind-weighting functions for  $^{12}\text{CO } J = 2-1$  line (day- and nightsides) are presented in Fig. 14, respectively. Wind sensitivity is primarily confined to the 85–110 km range. The altitude resolution indicated by the averaging kernels is consistent with the one indicated by the weighting

functions. Both, the weighting functions and the averaging kernels show a clear day/night dependence of the altitude in which the winds are detected. Vice versa, from the averaging kernels day and night observations can easily be identified. Fig. 6 shows wind retrievals for the Obs. 19, 20 and 21. Obs. 19 is pointing on the disc centre. The retrieved wind speed is zero as expected. Obs. 20 is pointing on the

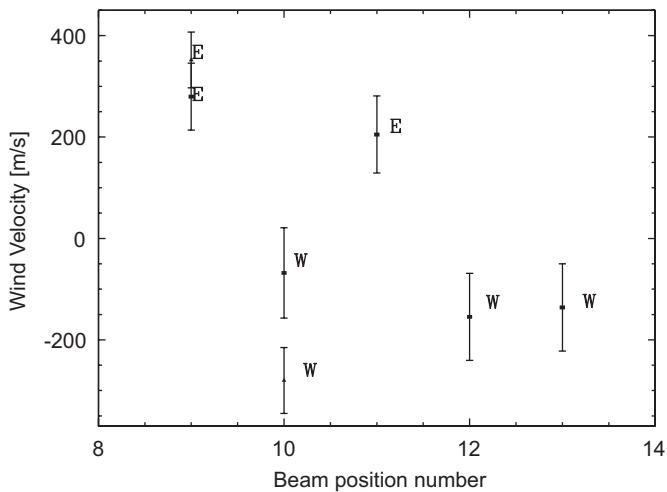


Fig. 15. Retrieved wind velocity measurements for different beam positions on the Venus' disc for two observing days. Squares: 14 June, triangles: 15 June. Retrieved velocity error bars are indicated. E: East, W: West.

nightside and provides a wind speed of nearly  $300 \text{ m s}^{-1}$  at 110 km altitude. The non-zero residual can be interpreted in a way, that for this observation the dayside emission is very weak and cannot compensate the emission from the nightside, therefore one-half of the double peak cannot be fitted. The wind of Obs. 22 is comparable with that of Obs. 20.

All the wind measurements given here are deprojected ones. Figs. 6–11 present all retrieved wind velocities, from two observing days (14 and 15 June), and Fig. 15 retrieved evident wind measurements as a function of beam position. In Fig. 15, when several observations were carried out at the same beam position and day (Obs. 20, 22 and 24 at beam position 9, Obs. 21 and 29 for beam position 10, and Obs. 25 and 27 for beam position 11), an averaged wind velocity is calculated (we assume that the beam is positioned at the same right ascension for the positions 9 and 14, and also for 10 and 15). Strong winds are also reported by Lellouch et al. (2008).

### 3.3. Characterization of the correlated errors

The optimal estimation method as described by Rodgers (1976) does not only allow to retrieve a temperature, mixing ratio, and wind profiles from the observed spectra of Venus, but in addition automatically provides an error estimate for the derived quantities. If each of the three profiles is represented by a set of  $n$  discrete numbers corresponding to  $n$  discrete layers representing the atmosphere of Venus, then the error estimation is given in the form of a covariance matrix  $S$  with the dimension  $3n \times 3n$ . Its diagonal elements are the variances of the profile values in each single layer and the square root of these variances is shown in Figs. 6–11 as error bars for the retrieved profiles. However, if the off-diagonal elements of  $S$  are not zero, they indicate a correlation of these errors, for example, the

temperature profile in a certain layer with the temperature errors within all the layers. In addition, the off-diagonal elements also specify the correlation between the temperature, mixing ratio and wind profile errors. In order to characterize these correlated errors we followed the formal procedure described in Rodgers (1990) and performed as an example an eigenvector  $\lambda$  and eigenvalue  $l$  analysis of  $S$  for the Obs. 34. This analysis provides the so-called error patterns (orthogonal quantities  $e_i = \lambda_i^{1/2} l_i$ ) which show the correlation of the errors for all retrieved quantities. There are in total  $3n$  error patterns and each single pattern consists of a part of  $n$  numbers belonging to the temperature,  $n$  numbers to the mixing ratio, and  $n$  numbers to wind profiles. Because these three blocks have different physical units for plotting purpose, a single pattern has been split and plotted into three separate panels (left, centre and right) in Figs. 16 and 17. Looking through all the error patterns suggests to sort them into three different groups: error patterns with large amplitudes for only (1) the temperature part, (2) the mixing ratio part, and (3) wind profile part. These three groups are shown in Fig. 16, upper, middle and lower panels. The fact that such a separation is possible shows that the errors of the three profiles are basically not correlated. The oscillating nature of part of the error patterns for the wind profile, for example, indicates the strong correlation between the wind profile errors in different layers. Looking at the error patterns with large amplitudes for the temperature reveals (1) the amplitudes are only large for altitudes outside the 70–100 km altitude range, showing that the CO spectral line contains enough information to significantly reduce the a priori profile error at this altitude; (2) there exists one error pattern which behaves exactly the opposite (see Fig. 16): it has a large amplitude within the 70–100 km range, but a small one outside. At the same time there is also a large error pattern amplitude for the CO profile part, which means that only in this case there is a strong correlation between the two errors. This single error pattern describes most of the error of the temperature profile in that altitude region, in which the observation is sensitive to atmospheric temperature. A further discussion of error patterns due to instrumental noise and null-space, and the effect of a priori data can be also based in the procedure described in Rodgers (1990), but this is beyond the scope of this paper.

## 4. Discussion

### 4.1. Short-term changes in the mesospheric thermal structure and in winds

We compare the day and night mesospheric temperature profiles from the 14 and 15 June observing period in Fig. 18. Direct detailed shape comparison indicates day-to-night and day-to-day small variations. For example, largest day-to-night variations of around 25 K occur at 102 km, day-to-day variations of around 15 K occur also at 85 km,

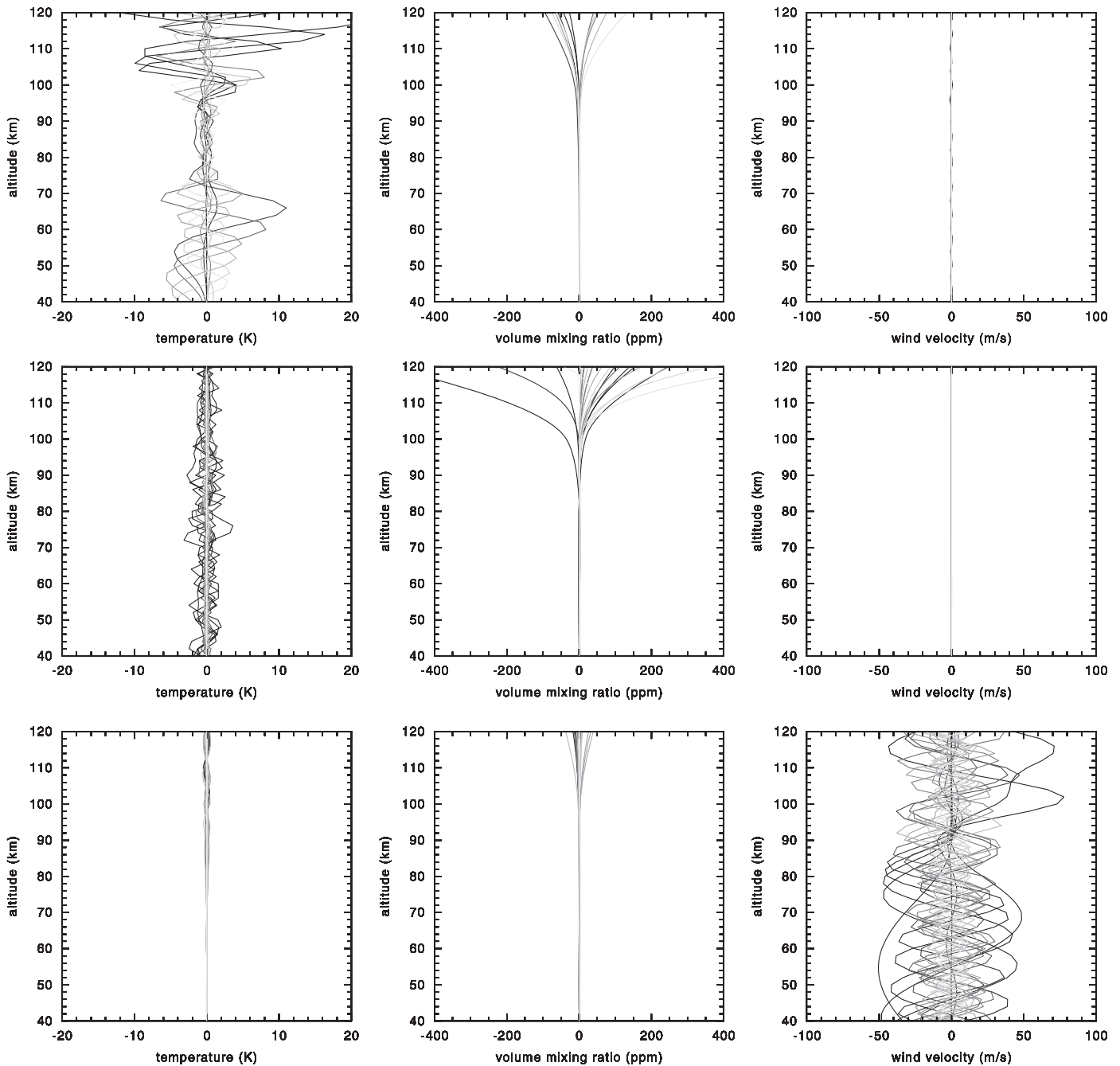


Fig. 16. Error patterns belonging to the temperature, mixing ratio and wind parts (upper, middle, and lower panels).

and night-to-night variations of around 15 K occur also at 102 km. It must be stressed however that any variation (spatial or temporal ones) is not differentiated here. Furthermore, measurements acquired at longer observing periods over the Venus' disc would define a pattern of variation (if any).

From Figs. 6–11, a qualitative comparison of the wind measurements suggests a day-to-day variability of the winds. For instance, for beam position 9, the velocity increases from around  $280 \text{ m s}^{-1}$  to around  $355 \text{ m s}^{-1}$  from 14 to 15 June, and for beam position 10, from  $-68$  to  $-280 \text{ m s}^{-1}$  from 14 to 15 June. From West-to-East limb

wind comparisons (at beam positions 10 and 13), we detect negative weaker winds of  $-68 \pm 89 \text{ m s}^{-1}$  and of  $-136 \pm 86 \text{ m s}^{-1}$ , respectively. Furthermore, at beam positions 9 and 11, we detect positive winds of  $280 \pm 66 \text{ m s}^{-1}$  and of  $205 \pm 76 \text{ m s}^{-1}$ , respectively. Wind measurements in Fig. 15 are taken at the wind peak of Figs. 6–11.

## 5. Conclusion

We have carried out several HHSMT  $^{12}\text{CO } J = 2-1$  and  $^{13}\text{CO } J = 2-1$  line observations on different beam positions on Venus disc during June 2007 around the MESSENGER

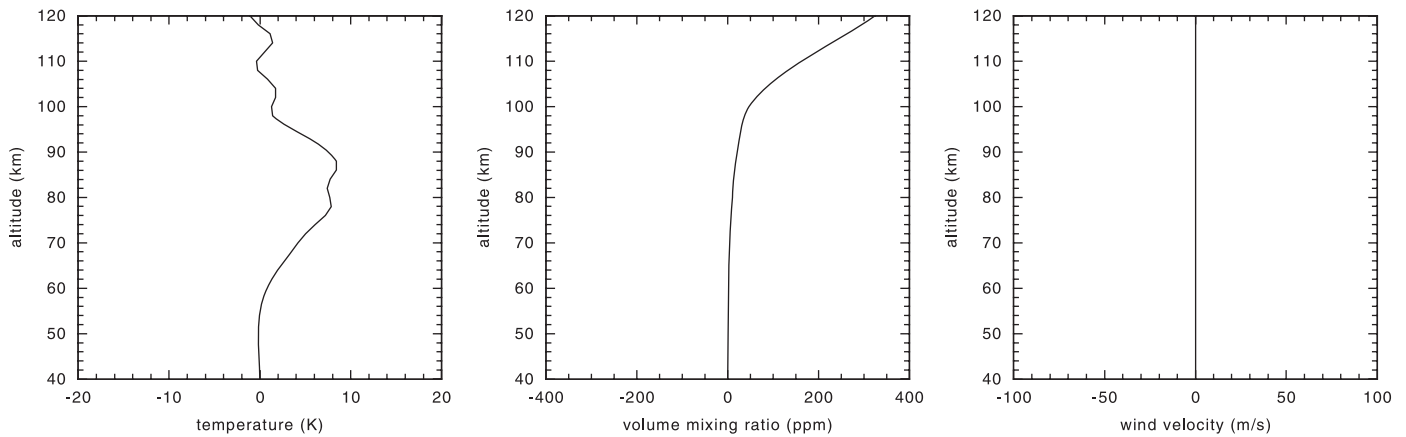


Fig. 17. Error patterns for the Obs. 34.

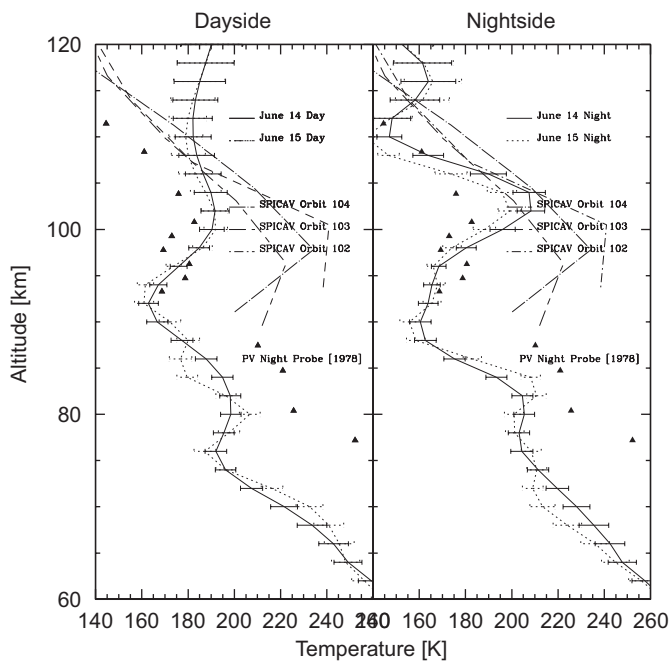


Fig. 18. Dayside (left) and nightside (right) HHSMT temperature profiles on 14 and 15 June (Obs. 29 and 34 for dayside with thin solid and dot-short dash lines, and Obs. 22 and 33 for nightside with thick solid and dot-short dash lines, respectively). Measurements from SPICAV (Bertaux et al., 2007) for orbits 102–104 are shown with dot-short, short dash-long, and dot-long dash lines, respectively, and from the PV night probe (Seiff et al., 1980) with triangles.

flyby of Venus and observations from Venus Express mission. From the spectra we retrieved vertical profiles of temperature, CO distribution, and wind velocities for the June 2007 mesosphere of Venus. Changes in the thermal structure of the Venus mesosphere are detected: day-to-night small temperature variations and short-term (day-to-day) on a time scale as short as one day. This is consistent with the picture of dramatic variability of the Venus mesosphere with changes in temperature occurring on short scales (Clancy et al., 2005; Sandor and Clancy, 2005). Furthermore, retrieved winds show variations of around

$100 \text{ m s}^{-1}$  between the winds on 14 June and those on 15 June.

HHSMT line observations of  $^{12}\text{CO}$   $J = 2-1$  and  $^{13}\text{CO}$   $J = 2-1$  and retrieved thermal profiles of the mesosphere of Venus (the temperature peak detection at 90–100 km) seems to support the new finding of the extensive layer of warm air detected by SPICAV onboard Venus Express.

Despite the success of the analysis presented here, some points need further work. Wind measurements and fluctuations of the zonal flow will be connected to possible CO distribution variability.

### Acknowledgements

We thank the staff of the HHSMT for crucial support while observing, and to J.-L. Bertaux and F. Montmessin for providing us the SPICAV data parallel to publication. We also thank the two manuscript referees for their criticism and valuable suggestions for improvement of the initial submission. We acknowledge JPL's Horizons online ephemeris generator for providing Venus's position during the observations. This research has made use of NASA's Astrophysics Data System.

### References

- Bertaux, J.-L., Vandaele, A.-C., Korablev, O., Villard, E., Fedorova, A., Fussen, D., Quémerais, E., Belyaev, D., Mahieux, A., Montmessin, F., Muller, C., Neefs, E., Nevejans, D., Wilquet, V., Dubois, J.P., Hauchecorne, A., Stepanov, A., Vinogradov, I., Rodin, A., Bertaux, J.-L., Nevejans, D., Korablev, O., Montmessin, F., Vandaele, A.-C., Fedorova, A., Cabane, M., Chassefière, E., Chaufray, J.Y., Dimarellis, E., Dubois, J.P., Hauchecorne, A., Leblanc, F., Lefèvre, F., Rannou, P., Quémerais, E., Villard, E., Fussen, D., Muller, C., Neefs, E., van Ransbeeck, E., Wilquet, V., Rodin, A., Stepanov, A., Vinogradov, I., Zasova, L., Forget, F., Lebonnois, S., Titov, D., Rafkin, S., Durry, G., Gérard, J.C., Sandel, B., 2007. A warm layer in Venus' cryosphere and high-altitude measurements of HF, HCl, H<sub>2</sub>O and HDO. *Nature* 450, 646–649.
- Clancy, R.T., Muhleman, D.O., 1991. Long-term (1979–1990) changes in the thermal, dynamical, and compositional structure of the Venus

- mesosphere as inferred from microwave spectral line observations of C-12O, C-13O, and CO-18. *Icarus* 89, 129–146.
- Clancy, R.T., Sandor, B.J., Moriarty-Schieven, G.H., 2003. Observational definition of the Venus mesopause: vertical structure, diurnal variation, and temporal instability. *Icarus* 161, 1–16.
- Clancy, R.T., Sandor, B.J., Moriarty-Schieven, G.H., 2005. Extreme Global Variability in the Middle Atmosphere of Venus. AGU Fall Meeting Abstracts, A223+.
- Gruszka, M., Borysow, A., 1997. Roto-translational collision-induced absorption of CO<sub>2</sub> for the atmosphere of Venus at frequencies from 0 to 250 cm<sup>-1</sup> at temperatures from 200 to 800 K. *Icarus* 129, 172–177.
- Hartogh, P., Hartmann, G.K., 1990. A high-resolution chirp transform spectrometer for microwave measurements. *Meas. Sci. Technol.* (1), 592–595.
- Hartogh, P., Jarchow, C., 2004. The microwave brightness of planetary atmospheres—preparatory modeling for GREAT and HIFI. In: Amano, T., Kasai, Y., Manabe, T. (Eds.), *Proceedings of the International Workshop on Critical Evaluation of mm-/submm-wave Spectroscopic Data for Atmospheric Observations*, January 29–30, 2004, Ibaraki, Japan. Communications Research Laboratory, pp. 75–78.
- Jarchow, C., 1998. Bestimmung atmosphärischer Wasserdampf- und Ozonprofile mittels bodengebundener Millimeterwellen- Fernerkundung. Ph.D. thesis.
- Jarchow, C., Hartogh, P., 1995. Retrieval of data from ground-based microwave sensing of the middle atmosphere: comparison of two inversion techniques. In: *Global Process Monitoring and Remote Sensing of Ocean and Sea Ice*, EUROPTO-Series 2586. SPIE, Bellingham, pp. 196–205.
- Kakar, R.K., Waters, J.W., Wilson, W.J., 1976. Venus—Microwave detection of carbon monoxide. *Science* 191, 379.
- Kliore, A.J., Keating, G.M., Moroz, V.I., 1992. Venus international reference atmosphere (1985). *Planet. Space Sci.* 40, 573.
- Lellouch, E., Goldstein, J.J., Rosenqvist, J., Bougher, S.W., Paubert, G., 1994. Global circulation, thermal structure, and carbon monoxide distribution in Venus' mesosphere in 1991. *Icarus* 110, 315–339.
- Lellouch, E., Paubert, G., Moreno, R., Moullet, A., 2008. Monitoring Venus' mesospheric winds in support of Venus express: IRAM 30-m and APEX observations. *Planet. Space Sci.*, Accepted for publication.
- Rengel, M., Hartogh, P., Jarchow, C., 2008. HHSMT Observations of the Venusian mesospheric temperature, winds, and CO abundance around the MESSENGER Flyby. *Planet. Space Sci.*, Accepted for publication.
- Rodgers, C.D., 1976. Retrieval of atmospheric temperature and composition from remote measurements of thermal radiation. *Rev. Geophys. Space Phys.* 14, 609.
- Rodgers, C.D., 1990. Characterization and error analysis of profiles retrieved from remote sounding measurements. *J. Geophys. Res.* 95, 5587–5595.
- Sandor, B.J., Clancy, R.T., 2005. Water vapor variations in the Venus mesosphere from microwave spectra. *Icarus* 177, 129–143.
- Schofield, J.T., Taylor, F.W., 1983. Measurements of the mean, solar-fixed temperature and cloud structure of the middle atmosphere of Venus. *Q. J. R. Meteorol. Soc.* 109, 57–80.
- Seiff, A., Kirk, D.B., 1982. Structure of the Venus mesosphere and lower thermosphere from measurements during entry of the Pioneer Venus probes. *Icarus* 49, 49–70.
- Seiff, A., Kirk, D.B., Young, R.E., Blanchard, R.C., Findlay, J.T., Kelly, G.M., Sommer, S.C., 1980. Measurements of thermal structure and thermal contrasts in the atmosphere of Venus and related dynamical observations—Results from the four Pioneer Venus probes. *J. Geophys. Res.* 85, 7903–7933.
- Villanueva, G., Hartogh, P., 2006. The high resolution chirp transform spectrometer for the SOFIA-GREAT instrument. *Exp. Astron.* 18, 77–91.
- Wilson, W.J., Klein, M.J., Kahar, R.K., Gulkis, S., Olsen, E.T., Ho, P.T.P., 1981. Venus. I—carbon monoxide distribution and molecular-line searches. *Icarus* 45, 624–637.